Three-Dimensional Mesoscale Heterostructures of ZnO Nanowire Arrays Epitaxially Grown on $CuGaO_2$ Nanoplates as Individual Diodes

Audrey Forticaux, Salih Hacialioglu, John P. DeGrave, Rafal Dziedzic, and Song Jin*

Department of Chemistry, University of Wisconsin—Madison, 1101 University Avenue, Madison, Wisconsin 53706, United States

ABSTRACT We report a three-dimensional (3D) mesoscale heterostructure composed of one-dimensional (1D) nanowire (NW) arrays epitaxially grown on two-dimensional (2D) nanoplates. Specifically, three facile syntheses are developed to assemble vertical ZnO NWs on $CuGaO_2$ (CGO) nanoplates in mild aqueous solution conditions. The key to the successful 3D mesoscale integration is the preferential nucleation and heteroepitaxial growth of ZnO NWs on the CGO nanoplates. Using transmission electron microscopy, heteroepitaxy was found between the basal planes of CGO nanoplates and ZnO NWs, which are their respective (001) crystallographic planes, by the observation of a hexagonal Moiré fringes pattern resulting from the slight mismatch between the *c* planes of ZnO and CGO. Careful analysis shows that this pattern can be described by a hexagonal supercell with a lattice parameter of almost exactly 11 and 12 times the *a* lattice constants for ZnO and CGO, respectively. The electrical properties of the individual CGO—ZnO mesoscale heterostructures were measured using a current-sensing atomic force microscopy setup to confirm the rectifying p—n diode behavior expected from the band alignment of p-type CGO and n-type ZnO wide band gap semiconductors. These 3D mesoscale heterostructures represent a new motif in nanoassembly for the integration of nanomaterials into functional devices with potential applications in electronics, photonics, and energy.

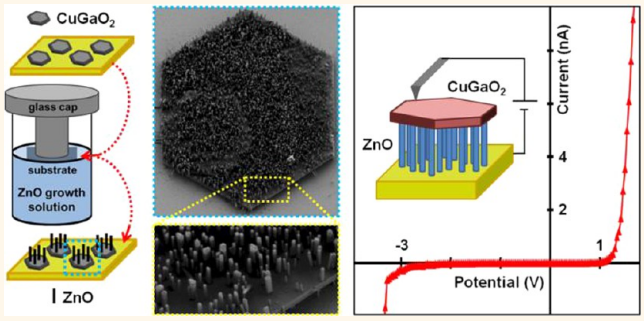

KEYWORDS: 3D heterostructure · nanowire · nanoplate · epitaxy · diode · mesoscale · ZnO

The rational synthesis and assembly of three-dimensional (3D) mesoscale structures from nanomaterial building blocks with well-defined properties is of great importance for numerous applications,[1−8] such as solar energy conversion,[1−3] electrochemical energy storage,[2,4] nanoelectronics,[2] nanophotonics,[5] and synthetic tissues.[6] For example, nanotrees (*i.e.*, branched nanowires (NWs)), are attractive for solar energy conversion because they combine one-dimensional (1D) properties, such as direct electron transfer path from the branches to the current collector, with 3D properties, in this case improved light trapping and high surface area for efficient solar energy harvesting and catalysis.[1,2,9−11] There are diverse bottom-up approaches to synthesize or assemble nanomaterials into 3D systems from simple mixing and/or deposition of nanomaterials[4,8,12] to direct gas or solution phase growth of hetero- and homostructures.[1,2,13−15] The variety of nanomaterial morphologies and compositions to build 3D structures is equally extensive. For example, 1D NWs can be assembled onto 2D surfaces[16−18] and then further built into 3D structures *via* layer-by-layer deposition.[12,19] By blending 1D NWs with other materials, 3D entangled networks[4,20] and aerogels[8] can be readily prepared. Furthermore, 3D hierarchical NW nanostructures can spontaneously grow in a single step[14,15,21] or can be synthesized through successive NW growth.[9,10,22−24] Going beyond 1D building blocks, combinations of nanostructures with 0D, 1D, and 2D dimensionalities can also lead to 3D mesoscale structures. Examples include zero-dimensional quantum dots decorating NW arrays,[3] "nanoflowers" made of two-dimensional (2D) nanoplates,[25] and 2D nanoplates grown on or mixed with 1D NWs.[12,26−28]

* Address correspondence to jin@chem.wisc.edu.

Received for review July 18, 2013 and accepted August 16, 2013.

Published online August 16, 2013
10.1021/nn4037078

The assembly or synthesis of 1D NWs on 2D nanostructures has rarely been explored.[29] Here, 2D nanostructures are broadly interpreted as nanostructures with a thickness of tens to hundreds of nanometers, or single layer, or sheet, of layered inorganic materials.[30,31] These 2D nano-objects are being investigated for a variety of applications, such as high-performance nanoelectronic and optoelectronic devices,[31] topological insulators,[32,33] dielectrics,[30,34] plasmonics,[35,36] catalysis,[35] and supercapacitors.[37,38] These 2D structures are also convenient platforms for incorporating new materials,[39] which led us to the idea of single integrated devices composed of a stand-alone 2D nanoplate decorated with 1D NWs. This approach to form an individual 3D mesoscale heterostructure represents a new motif in nanoassembly for the integration of nanocomponents by taking advantages of both 2D and 1D nanoscale geometries and properties to form functional devices.

Here, we report the synthesis of 3D mesoscale heterostructures of 1D ZnO NW arrays epitaxially grown on 2D $CuGaO_2$ (CGO) nanoplates in aqueous solution. CGO has the rhombohedral delafossite crystal structure (JCPDS #41-0255; space group $R\bar{3}m$, a = 2.976 Å, c = 17.158 Å in the hexagonal crystallographic setting), and ZnO has the hexagonal wurtzite structure (JCPDS # 36-1451; space group $P6_3mc$, a = 3.25 Å, c = 5.207 Å). *A priori* the basal planes of CGO nanoplates and ZnO NWs are their respective (001) crystallographic planes, that is, their *c* planes,[40−43] and therefore, a heteroepitaxial relationship at this interface is highly probable since their *a* lattice parameters are only mismatched by 10%. Furthermore, CGO and ZnO have complementary properties. As a p-type semiconductor with a wide band gap of ~3.6 eV, CGO has been investigated as a photocathode material in p-type dye-sensitized solar cells[42,44] and as a promising p-type transparent conducting oxide (TCO) material[45] since it has almost the same band gap and crystal structure as $CuAlO_2$, a material extensively studied as one of the most promising p-type TCO.[46] ZnO is a n-type semiconductor with a wide band gap of 3.2 eV and is useful for many applications, such as photonics,[47] and solar,[48] and piezoelectric[49] energy conversion. The n-type ZnO and p-type $CuAlO_2$ can form a type II staggered band alignment,[50] thus it is likely that each individual CGO nanoplate−ZnO NW array 3D heterostructure could be a p−n junction diode. However, unlike $CuAlO_2$, the growth of high-quality crystalline CGO thin films has not been well-developed.[45]

In this article, we take advantage of some well-defined large single-crystal CGO nanoplates that we have synthesized *via* hydrothermal reaction[41] and our expertise in solution-grown ZnO NWs[40,43] to develop three facile synthetic routes to controllably assemble ZnO NW arrays on CGO nanoplates to form 3D mesoscale heterostructures in mild aqueous solution conditions. One of these routes also exploits the ability of nanoplates to float on top of aqueous solutions,[18,51]

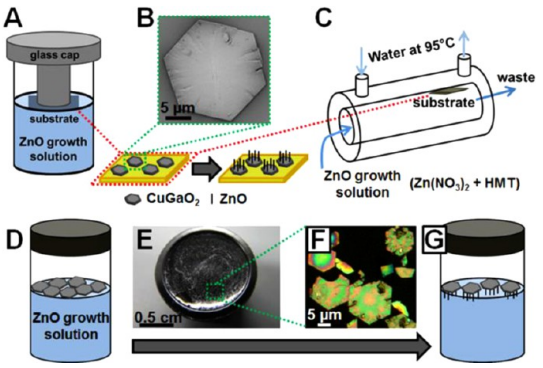

Figure 1. Schemes illustrating the three different synthesis methods to grow ZnO NW arrays on CGO nanoplates. (A) "Suspended" synthesis: CGO nanoplates are deposited on a gold-coated Si/SiO_2 substrate, as shown in the SEM image (B), which is then taped to a glass cap and immersed (facing down) in the ZnO precursor solution to grow the NW array; (C) CFR method; (D−G) "floating" synthesis: CGO nanoplates float on top of the ZnO growth solution as shown in the digital photograph (E) and bright-field optical micrograph (F).

leading to free-floating heterostructures. These well-defined 3D mesoscale heterostructures are characterized by scanning electron microscopy (SEM), and the epitaxial relationship between CGO and ZnO is confirmed and elucidated by transmission electron microscopy (TEM). Finally, we measure the electrical properties of the CGO−ZnO heterostructures using a current-sensing atomic force microscopy (CSAFM) setup and show their p−n junction diode characteristics.

RESULTS AND DISCUSSION

Synthesis of the CGO Nanoplate−ZnO NW Array Heterostructures. CGO nanoplates were grown *via* a hydrothermal reaction by improving a procedure found in the literature.[41] Lower concentrations of precursors (*i.e.*, lower supersaturation for crystal growth)[52] and/or a different precursor of ethylene diamine as the reductant were employed in our synthesis instead of the ethylene glycol used in the reported synthesis. These modifications consistently led to single-crystal nanoplates with a much larger lateral dimension compared to the previous reports, in which only platelets of a few hundred nanometers in width were synthesized.[41] After appropriate washing and rinsing, the nanoplates were confirmed to be phase pure CGO by powder X-ray diffraction (PXRD, Supporting Information Figure S1). SEM (Figure 1B) showed that the single-crystal CGO nanoplates have well-defined hexagonal crystal shapes and an average diameter of 20 μm, and their thickness ranges from 20 to 350 nm depending on the synthetic conditions.

For the heterostructure syntheses, the growth of ZnO NW arrays was performed in three different ways. In the first method called "suspended" synthesis (Figure 1A), nanoplates dispersed in ethanol were drop-casted on a gold-coated Si/SiO_2 substrate which

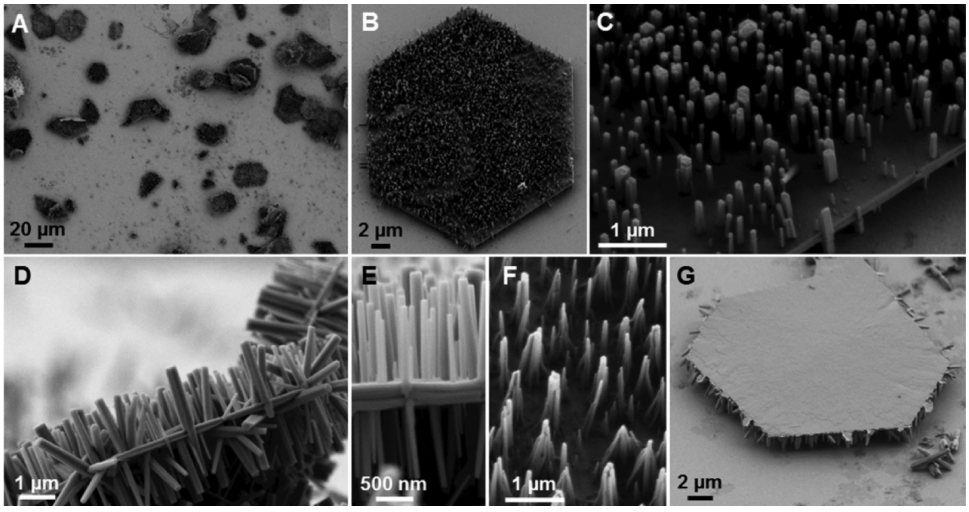

Figure 2. SEM images of CGO nanoplate−ZnO NW array heterostructures. Heterostructures grown *via* the "suspended" synthesis (A−E), CFR (F), and the "floating" synthesis (G).

was then immersed, facing down, just below the air−water interface of the precursor solution for ZnO growth (10 mM zinc nitrate and 10 mM hexamethylenetetramine (HMT)). The solution was then heated at 90 °C for 1 h to grow ZnO NWs. In the second method (Figure 1C), similar substrates as in the first method were mounted facing down in a continuous flow reactor (CFR), a process we previously developed to promote the screw dislocation-driven growth of NWs at low supersaturation[40,53,54] and to enable controllable growth of high aspect ratio ZnO NWs. The third method, called the "floating" synthesis (Figure 1D−G) was inspired from two recent studies. In the first report, when nanoplates of β-$Co(OH)_2$ were dispersed in ethanol and drop-casted on top of an aqueous solution; they moved to the water−ethanol interface and self-assembled into a floating monolayer.[18] In the second one, a free-floating seed layer of ZnO was formed *in situ* on the surface of the precursor solution, which then initiated the ZnO NW growth downward into a self-supported NW array.[55] Here, as illustrated in Figure 1D, CGO nanoplates dispersed in ethanol and drop-casted on top of the ZnO precursor solution also formed a floating layer, which was directly visible by eye (Figure 1E), and the free-standing CGO nanoplates could be observed by optical microscopy (Figure 1F). The floating CGO nanoplate layer was preserved when the precursor solution was heated to 90 °C to enable ZnO NW growth downward into the solution (Figure 1G). Finally, the heterostructures were scooped on a gold-coated Si/SiO_2 substrate for further characterization.

SEM images reveal that after the "suspended" synthesis, CGO nanoplates are completely covered by dense vertical arrays of rather uniform ZnO NWs with diameters ranging from 100 to 250 nm and heights of about 1.5 μm (Figure 2A−C). Note that when the nanoplates are not lying perfectly horizontal, ZnO NWs can grow on both sides of the nanoplates (Figure 2D,E). The absence of ZnO growth on the gold-coated Si/SiO_2 substrate at this high precursor concentration (10 mM) already suggests that there is preferential nucleation and growth of ZnO on CGO nanoplates.[56] Note that when the ZnO precursor concentration is doubled, supersaturation increases and the heterogeneous nucleation on the gold surface becomes possible; therefore, ZnO NWs also grow on the gold-coated Si/SiO_2 substrate but with a much lower density in comparison to the CGO nanoplates (Figure S2A).

We can also grow thinner ZnO NWs by reducing the precursor concentration. However, reducing the concentration by half in the suspended synthesis leads to a poor NW coverage on the nanoplates (Figure S2B). Therefore, instead of using the suspended synthesis, which is a static hydrothermal reaction leading to convoluted crystal growth regimes as the precursors are being depleted, we used the CFR method to maintain a constant low supersaturation[40] and grow thinner ZnO NWs with diameters ranging from 20 to 50 nm and larger aspect ratios. Interestingly, these thinner NWs could collapse on each other, forming teepee-like structures (Figure 2F) or dramatic entangled networks of longer NWs (Figure S3A) due to their close proximity and surface tension effect.[57] Note that under this low precursor concentration no ZnO NWs grew on the gold-coated Si/SiO_2 substrate (Figure S3B).

Finally, with the floating synthesis, the heterostructures scooped on a gold-coated Si/SiO_2 substrate are "inverted"; that is, NWs are in contact with the conducting substrate, and the nanoplate is on top of the mesoscale object (Figure 2G). This is an important geometric advantage for studying the electrical properties of the CGO−ZnO junction as discussed later.

Epitaxial Relationship between CGO Nanoplates and ZnO NWs. To understand the preference for ZnO NWs to nucleate and grow vertically on CGO nanoplates, we used TEM to investigate the epitaxial relationship

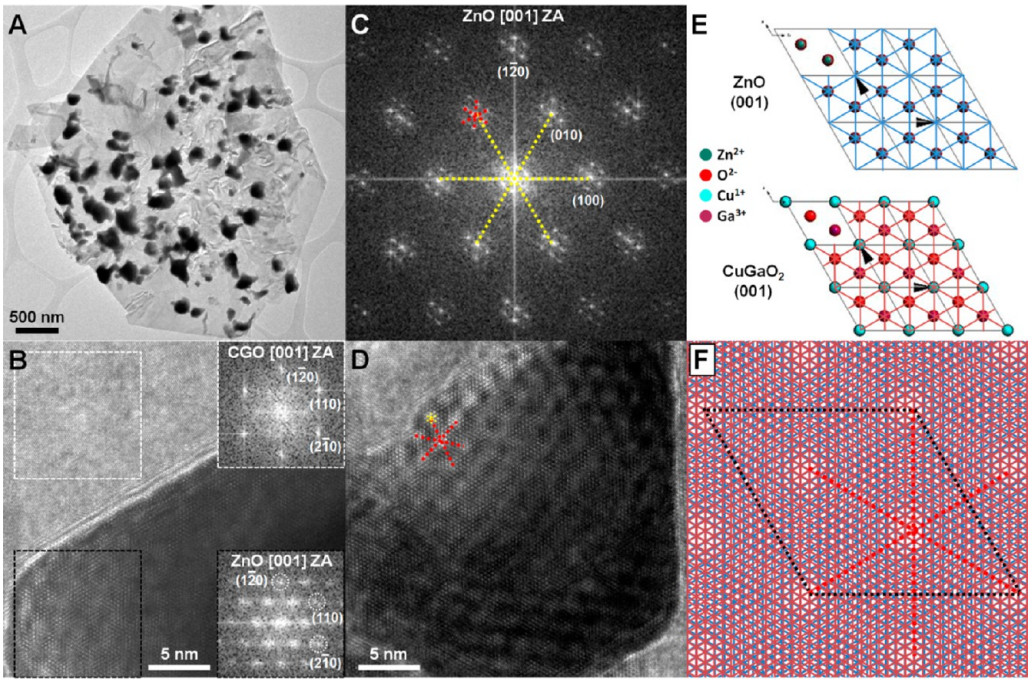

Figure 3. Epitaxial relationship between CGO nanoplate and ZnO NW, top-down view. (A) Low-magnification TEM of the heterostructure in top-down view. (B) HRTEM image of the CGO nanoplate−ZnO NW heterostructure basal plane and the indexed FFTs corresponding to different areas. (C) FFT of a well-resolved HRTEM image (D) of the CGO−ZnO overlapped area with a distinct hexagonal Moiré fringes pattern; the yellow dashes highlight the ZnO lattice, and the red dashes highlight the Moiré fringes pattern. (E) Representations of the (001) planes of ZnO and CGO crystal structures. (F) Illustration of the emergence of the Moiré fringes pattern and the heteroepitaxial relationship by overlapping the (001) planes of CGO (red) and ZnO (blue). The hexagonal supercell with a lattice constant *a* of 3.57 nm is highlighted with black dashes, and the hexagonal Moiré fringes pattern is highlighted with red dashes with a of spacing 2.06 nm.

between CGO nanoplates and ZnO NWs. As TEM requires thin samples, we examined the heterostructures grown *via* CFR on small and thin CGO nanoplates. When a nanoplate of a few micrometers in diameter is viewed perpendicularly to its basal plane (Figure 3A), the clearest areas in the TEM images (*i.e.*, the thinnest material) correspond to the CGO nanoplate, and the dark spots (*i.e.*, the thickest material) correspond to ZnO NWs viewed head-on. The NWs are mostly broken off during sample preparation, which makes the interface thin enough to acquire high-resolution TEM (HRTEM) images and their corresponding fast Fourier transforms (FFTs). A representative HRTEM image of the basal plane of the CGO−ZnO heterostructure (Figure 3B) shows that CGO and ZnO are both single crystalline and the FFT of the clear area indexes to the [001] CGO zone axis while the FFT for the dark area indexes to the [001] ZnO zone axis. Hence the basal plane of both materials is their respective (001) crystallographic planes where the interface between CGO and ZnO lies. The generality of the heteroepitaxy over many structures is further supported by PXRD done on as-synthesized heterostructures lying down on the substrate, which displays a dramatic enhancement of the (00*l*) peaks (Figure S1). While it makes sense to only see CGO in the clear area in the HRTEM image, we expected to find both ZnO and CGO in the dark area as the two materials overlap. Closer examination reveals modulated features in the HRTEM image and diffused spots in the corresponding FFT (Figure 3B). In fact, each of these spots is surrounded by six satellite spots arranged hexagonally (red dashes) as shown in the FFT (Figure 3C) of a more distinct HRTEM image from a different object, which clearly shows an additional honeycomb-like contrast modulation on top of the resolved hexagonal lattice fringe with a spacing of about 2.1 nm (red dashes, Figure 3D). The modulation in the TEM image is called Moiré fringes. Moiré fringes are essentially an interference pattern due to the overlap of two lattice planes, such as two mismatched lattice planes, or two identical planes that are slightly staggered or with a rotation angle between them. To understand the observed Moiré fringes (Figure 3D), we examined the CGO and ZnO crystal structures projected on their (001) planes and represented the major lattice planes as simple lines (Figure 3E). By overlapping these families of lattice planes, we obtained a simulated hexagonal pattern with a spacing of 2.06 nm from the central dot (red dashes, Figure 3F) that matches the modulated features in the HRTEM image. The overlapped superstructure can be described by a supercell with a lattice parameter *a* of 3.57 nm (black dashes, Figure 3F), which is almost exactly 11 ZnO and 12 CGO unit cells along the *a* direction, that is, $11 \times a_{ZnO} = 11 \times 0.325$ nm = 3.575 nm and $12 \times a_{CGO} = 12 \times 0.2976$ nm = 3.571 nm. Therefore, the interpretation of

the Moiré fringes confirms the epitaxial relationship between the *c* planes of CGO and ZnO.

Since the basal plane is (001), the perpendicular direction [001] is the growth direction of both CGO nanoplates[41,42] and ZnO NWs,[40] which is consistent with the literature. To confirm this and obtain additional information on the interface between the two materials, we further characterized the CGO nanoplate–ZnO NW heterostructures parallel to their basal plane (side view) under TEM. To this end, we found fragments of the heterostructures with a thin enough CGO nanoplate portion still attached to a ZnO NW from which fully lattice-resolved HRTEM images can be obtained (Figure 4A) or partially resolved with the most important [001] direction perpendicular to the heterostructure interface (Figure 4B). These HRTEM images and their corresponding FFTs confirm that the growth direction of CGO and ZnO is [001] and the interface lies on their respective (001) planes. The similarity in the crystal structure of the two compounds is quite apparent in the lattice-resolved TEM images and corresponding FFTs (Figure 4A). An energy-dispersive X-ray spectroscopy (EDX) elemental map by scanning TEM (STEM) also confirms the sharpness of the interface between zinc, which is only present on the NW side, and copper and gallium, which are only present on the nanoplate side in a homogeneous way (Figure 4C).

The key to the successful 3D integration is the preferential nucleation and heteroepitaxial growth of 1D NWs on 2D nanoplates. As we know from previous work, the solution growth of ZnO NWs is driven by screw dislocations,[40] which may indicate that sources of defects on the CGO nanoplate surface, such as screw dislocations, initiated the growth of ZnO NWs, as in the case of ZnO NWs grown on a dislocated GaN thin film.[43] Thus, we investigated the presence of defects on the CGO nanoplate surface and observed spirals in thin CGO nanoplates by SEM (Figure S4A,B), as well as an overall squashed pyramidal shape for thick CGO nanoplates by AFM (Figure S4C,D), which are two characteristics seen in screw dislocation-driven nanoplates.[52,58] These observations suggest that screw dislocation defects in CGO plates could also be responsible for the preferential nucleation and growth of ZnO NWs; however, there was not enough evidence, such as the observation of threading dislocations, to fully confirm this growth mechanism. The preferential heteroepitaxial growth of ZnO NWs from CGO nanoplates and the likely dislocation-driven growth eliminate the use of ZnO seed layers and the need to define the locations of such seed layers (as often done in other studies of ZnO NW growth) to successfully achieve these 3D mesostructures.

Electrical Properties of 3D CGO Nanoplate–ZnO NW p–n Diodes. As mentioned in the introduction, CGO and ZnO are respectively p-type and n-type wide band gap semiconductors, and their relative band positions make a type II staggered band alignment, with p-type

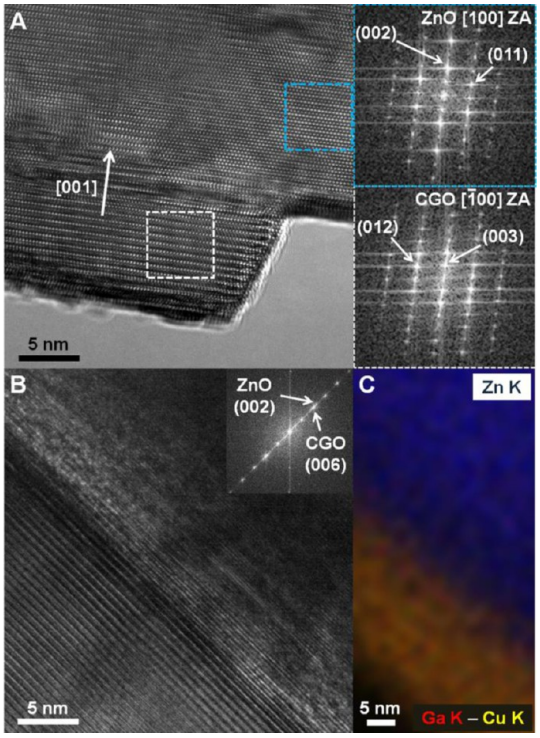

Figure 4. Epitaxial relationship between CGO nanoplate and ZnO NW, side view. (A) Fully lattice-resolved HRTEM of the interface between a CGO nanoplate and a ZnO NW with indexed FFTs of each side of the heterostructure highlighting the epitaxial relationship along their (001) planes. (B) HRTEM and FFT of a partially resolved heterostructure showing the most important [001] direction perpendicular to the heterostructure interface. (C) EDX elemental mapping of the interface from (B) displaying the sharp transition between CGO and ZnO.

CGO band position[59] higher than n-type ZnO (Figure 5A). Therefore, the resulting p–n junction is expected to show a rectifying diode behavior, as illustrated in the energy band diagrams in Figure 5B for different bias conditions.[45,46,50] Note that this illustration is highly schematic because the exact positions of the Fermi levels within the CGO and ZnO bands are not known but captures the qualitative picture.

In order to measure the electrical properties of these CGO–ZnO heterostructures, we took advantage of a CSAFM setup to measure individual 3D heterostructures with minimal sample preparation and sample damage. In a typical CSAFM measurement, a conductive Pt-coated AFM tip held at virtual ground is in contact with the sample on a conductive substrate that is connected to a voltage source, and when a bias voltage is applied, a current is measured as it flows through the AFM tip. The heterostructures grown *via* the floating synthesis are the most convenient samples to study with the NWs in contact with the conducting gold-coated Si/SiO_2 substrate and the nanoplate on top of the assembly as described earlier (SEM in Figure 5B inset). With this measurement geometry, the conductive AFM tip scans and electrically contacts the surface of the nanoplate (scheme in Figure 5C inset),

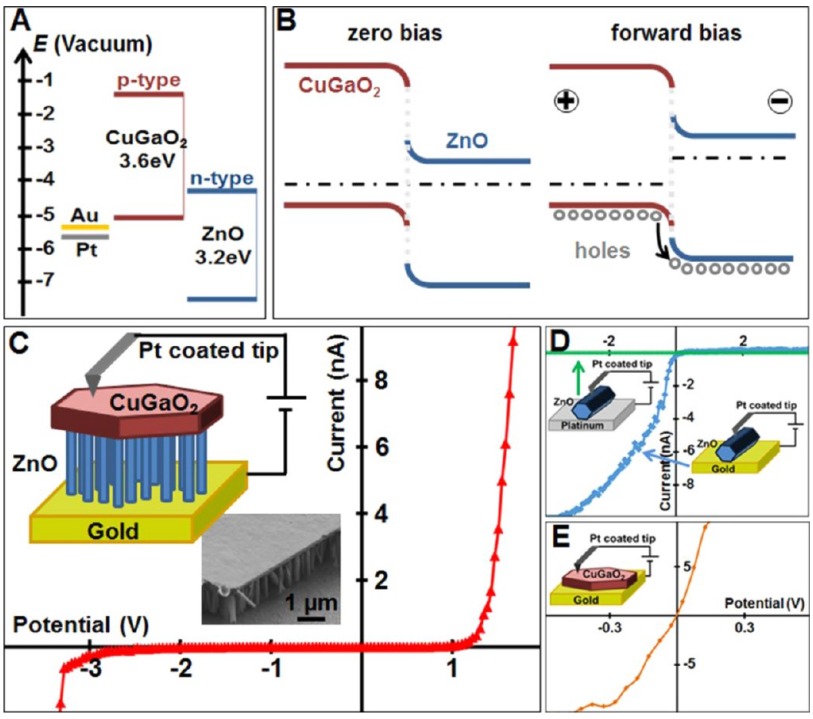

Figure 5. Diode behavior of individual 3D CGO nanoplate−ZnO NW array device measured by CSAFM. (A) Band diagram between p-type CGO and n-type ZnO and work functions of the metal contacts, Au and Pt. (B) Schematic of the band bending at the heterostructure interface between p-type CGO and n-type ZnO at zero and forward biases. (C) Representative *I*−*V* curve of the CGO nanoplate−ZnO NW heterostructures annealed at 350 °C for 1 h showing its diode behavior (insets show the scheme of the measurement setup and a representative SEM image of the heterostructure); control measurements on annealed single components of the junction: ZnO NWs (D) and CGO nanoplates (E).

which is easier than scanning the NW tips and is more reliable as neither the AFM tip nor the sample will be damaged during the measurement. Furthermore, with this configuration, we directly measure the diode behavior of the junction in forward bias as expected from the band diagram.

A representative *I*−*V* curve for CGO nanoplate−ZnO NW array heterostructures annealed at 350 °C for 1 h in air shows a turn-on voltage of +1.5 V and a breakdown voltage of −3.3 V (Figure 5C). A total of eight heterostructures were measured, and all displayed similar *I*−*V* characteristics. To ensure that this is a true diode behavior and does not come from non-ohmic contact between the components of the structure and the metal contacts, we also measured the *I*−*V* characteristics of individual ZnO NWs (Figure 5D) and CGO nanoplates (Figure 5E) that were also annealed at 350 °C for 1 h in air after being drop-casted on conducting substrates. We first recorded the *I*−*V* curve of ZnO NWs on a gold-coated Si/SiO_2 substrate using a Pt-coated tip as we used for the heterostructures. A rectifying behavior was observed with current passing through the Pt−ZnO−Au junction under negative bias (Figure 5D, blue curve), basically the opposite of what was observed for the CGO−ZnO heterostructures. This is due to a Pt−ZnO metal−semiconductor Schottky junction diode.[60] This is further confirmed by the observation of a flat *I*−*V* curve on ZnO NWs on a platinum-coated Si/SiO_2 substrate measured using a Pt-coated AFM tip (Figure 5D, green curve). Now the barrier between Pt and ZnO is on both sides, that is, a Pt−ZnO−Pt junction. In any case, it is clear that the rectifying behavior observed for the heterostructures cannot come from ZnO alone. Additionally, when CGO nanoplates on gold-coated Si/SiO_2 substrate were measured using a Pt-coated AFM tip, linear *I*−*V* curves were observed, indicating ohmic contact (Figure 5E). Considering that we have ohmic contacts between ZnO and Au and between CGO and Pt, the rectifying behavior observed for the heterostructure Pt AFM tip−CGO nanoplate−ZnO NWs−Au is due to the CGO nanoplate−ZnO NW p−n junction, which confirms the diode behavior expected from the band diagram.

CONCLUSION

In conclusion, we reported a new 3D mesoscale heterostructure composed of 1D ZnO NW arrays heteroepitaxially grown on 2D CGO nanoplates synthesized in mild aqueous solutions. Under TEM, we confirmed the heteroepitaxy between the basal planes of CGO nanoplates and ZnO NWs, which are their respective (001) planes. The overlap of these two slightly mismatched lattice planes generates a hexagonal Moiré fringes pattern under TEM, which can be described by a supercell with a lattice parameter *a* of

3.57 nm. The electrical properties of individual CGO nanoplate−ZnO NW array p−n junctions, measured with a CSAFM setup, showed a diode behavior as expected from the band alignment of p-type CGO and n-type ZnO. The key to obtain these 3D mesoscale structures is the preferential nucleation and heteroepitaxial growth of ZnO NWs on CGO nanoplates. These heterostructures represent a new motif for nanoassembly into 3D mesoscale architectures. The general approach demonstrated herein with the specific example of CGO−ZnO opens up the development of other 3D mesoscale heterostructures built from diverse 2D and 1D nanomaterials in the future for the integration of nanoscale building blocks into functional devices with potential applications in electronics, photonics, energy conversion, and storage.

METHODS

Chemicals were purchased from Sigma-Aldrich and used as received unless otherwise stated.

CGO Nanoplate Synthesis. The procedure was modified from the literature.[41] Briefly, 181.2 mg of $Cu(NO_3)_2 \cdot 3H_2O$ (0.75 mmol), 191.8 mg of $Ga(NO_3)_3 \cdot xH_2O$ (from 0.75 mmol with $x = 0$ to 0.70 mmol with $x = 1$), and 210.4 mg of KOH (3.75 mmol) were dissolved in 15 mL of nanopure water (Thermo Scientific, Barnstead Nanopure, 18.2 MΩ·cm). Then, 1.00 mL of ethylene glycol (Fisher) was added to 7.5 mL of this solution, and the total volume was brought up to 15 mL with nanopure water. The resulting solution was sealed in a 23 mL autoclave and heated at 200 °C for 60−73 h in a convection oven. Instead of ethylene glycol, 150 μL of ethylene diamine was also used to obtain thicker and larger nanoplates, and the reaction could then be finished in only 2 h. After the reactions, the products were washed successively with nanopure water, ethanol, concentrated ammonia, 0.5 M HNO_3, nanopure water, and finally ethanol and dried at 60 °C overnight.

Growth of ZnO NW Arrays on CGO Nanoplates. CGO nanoplates were dispersed in ethanol, and the growth of ZnO NWs was performed in three different ways:

"Suspended" Synthesis. CGO nanoplates were drop-casted on a 1 cm by 1 cm Si substrate with 600 nm of thermally grown SiO_2 that was coated with 15 nm Ti and then 50 nm Au by metal evaporation. This substrate was then taped on a glass cap and immersed just below the air−water interface, facing down, in a glass vial containing 17 mL of freshly prepared precursor solution for ZnO growth, which consists of 8.5 mL of $Zn(NO_3)_2 \cdot 6H_2O$ at 20 mM mixed less than 1 min before growth with 8.5 mL of hexamethylenetetramine (HMT) at 20 mM in nanopure water. Then, the glass vial was heated at 90 °C for 1 h to allow the ZnO NW growth. The substrate was then rinsed with ethanol and dried in a flow of N_2 gas.

Continuous Flow Cell Reactor (CFR) Synthesis. The CFR setup has been previously detailed;[40] therefore, we will only mention the important parameters. Here, 1 cm by 2.5 cm substrate covered with CGO nanoplates, as prepared as in the suspended synthesis, was mounted facing down in a clean jacketed chromatography column (*i.e.*, the CFR column). When the CFR column temperature was warmed to 95 °C, the two freshly prepared precursor solutions, 500 mL of zinc nitrate at 100 μM and 500 mL of HMT at 100 μM in nanopure water, were pumped into the column using a peristaltic pump. Just before the solution started to immerse the substrate, the flow was temporarily stopped to allow the solution to warm for 20 min. Then, the CFR column was quickly filled up, and the precursor solution flowed at a total speed of 1.6 mL/min (*i.e.*, 0.8 mL/min for each precursor) for 4 h. At the end of the reaction, the heating and the flow were stopped, and the substrate was quickly removed from the column, rinsed with ethanol, and dried in a flow of N_2 gas.

"Floating" Synthesis. This synthesis is very similar to the suspended synthesis except that the CGO nanoplates dispersed in ethanol were directly drop-casted on top of the ZnO growth solution forming a free-floating layer. After ZnO NW growth, the heterostructures were scooped on a 1 cm by 2 cm gold-coated Si/SiO_2 substrate with no additional rinsing.

Structural Characterization. The powder X-ray diffraction (PXRD) patterns of as-synthesized CGO nanoplates deposited on glass and as-synthesized CGO−ZnO heterostructures *via* the suspended synthesis on a gold-coated Si/SiO_2 substrate were collected on a Bruker D8 Advance powder X-ray diffractometer using Cu Kα radiations. For scanning electron microscopy (SEM), drop-casted samples or as-synthesized heterostructures on substrates were mounted onto metal pucks with double-sided carbon tape and imaged using a LEO Supra 55 VP field emission SEM. In a typical transmission electron microscopy (TEM) sample preparation, ZnO−CGO heterostructures were wiped off the substrate surface with a clean room wipe wetted with ethanol in order to mildly fragment them, then the wipe was placed in ethanol in a 1.5 mL centrifuge tube to release the heterostructures. Then, a few drops of the suspension were casted on a TEM grid (Ted Pella, lacey carbon type-A support film, 300 mesh, copper, #01890-F) and allowed to dry. TEM was carried out on a FEI Titan transmission electron microscope at an accelerating voltage of 200 kV. Energy-dispersive X-ray spectroscopy (EDX) elemental mapping was performed on the same instrument in scanning TEM (STEM) mode for higher resolution at 200 kV.

Electrical Measurements Using Current Sensing Atomic Force Microscopy (CSAFM). In a typical sample preparation, a copper wire was bonded with silver epoxy to contact the conductive surface of the substrate to the current source of an Agilent 5500 AFM instrument. To make the second contact to the sample, conductive Pt-coated AFM tips were used (MikroMasch, HQ:XSCII/Pt, 30 nm Pt coating, tip radius <30 nm, the most common tip used on these four-lever probes has a resonance frequency of 80 kHz, and a spring constant of 2.7 N/m). The AFM tip was linked to a preamplifier with a sensitivity of 1 nA/V and a measurable current range from −10 to +10 nA before signal saturation. A minimum of five *I*−*V* sweeps were taken for at least two different locations on each examined object. The ZnO−CGO heterostructures from the floating synthesis, scooped on gold-coated Si/SiO_2 substrates and annealed at 350 °C for 1 h in air in a box furnace, were used for these measurements. For the control measurements on CGO nanoplates, samples were prepared as in the first step of the suspended/CFR syntheses on gold-coated Si/SiO_2 substrates and annealed at 350 °C for 1 h in air. For ZnO, NWs were synthesized as in the suspended synthesis, that is, in a precursor solution of 10 mM $Zn(NO_3)_2 \cdot 6H_2O$ and 10 mM HMT, but without any substrate. Instead, the ZnO NW products were centrifuged, washed with ethanol, and drop-casted on a gold- or platinum-coated Si/SiO_2 substrate and then annealed at 350 °C for 1 h in air.

Conflict of Interest: The authors declare no competing financial interest.

Acknowledgment. This research is supported by the University of Wisconsin—Madison NSEC (NSF DMR 0832760). S.H. was partially supported by a Fulbright Fellowship. S.J. also thanks the Research Corporation SciaLog Award for Solar Energy Conversion and UW-Madison Vilas Associate Award for support.

Supporting Information Available: Additional SEM and AFM images of CGO nanoplates and their PXRD pattern, and additional SEM images of the ZnO NW−CGO nanoplate heterostructures grown by the "suspended" and CFR syntheses, and their PXRD pattern. This material is available free of charge *via* the Internet at http://pubs.acs.org.

REFERENCES AND NOTES

1. Bierman, M. J.; Jin, S. Potential Applications of Hierarchical Branching Nanowires in Solar Energy Conversion. *Energy Environ. Sci.* **2009**, *2*, 1050–1059.
2. Cheng, C. W.; Fan, H. J. Branched Nanowires: Synthesis and Energy Applications. *Nano Today* **2012**, *7*, 327–343.
3. Selinsky, R. S.; Ding, Q.; Faber, M. S.; Wright, J. C.; Jin, S. Quantum Dot Nanoscale Heterostructures for Solar Energy Conversion. *Chem. Soc. Rev.* **2013**, *42*, 2963–2985.
4. Li, L.; Meng, F.; Jin, S. High-Capacity Lithium-Ion Battery Conversion Cathodes Based on Iron Fluoride Nanowires and Insights into the Conversion Mechanism. *Nano Lett.* **2012**, *12*, 6030–6037.
5. von Freymann, G.; Kitaev, V.; Lotschz, B. V.; Ozin, G. A. Bottom-Up Assembly of Photonic Crystals. *Chem. Soc. Rev.* **2013**, *42*, 2528–2554.
6. Tian, B. Z.; Liu, J.; Dvir, T.; Jin, L. H.; Tsui, J. H.; Qing, Q.; Suo, Z. G.; Langer, R.; Kohane, D. S.; Lieber, C. M. Macroporous Nanowire Nanoelectronic Scaffolds for Synthetic Tissues. *Nat. Mater.* **2012**, *11*, 986–994.
7. Joshi, R. K.; Schneider, J. J. Assembly of One Dimensional Inorganic Nanostructures into Functional 2D and 3D Architectures. Synthesis, Arrangement and Functionality. *Chem. Soc. Rev.* **2012**, *41*, 5285–5312.
8. Jung, S. M.; Jung, H. Y.; Dresselhaus, M. S.; Jung, Y. J.; Kong, J. A Facile Route for 3D Aerogels from Nanostructured 1D and 2D Materials. *Sci. Rep.* **2012**, *2*, 849.
9. Hwang, Y. J.; Wu, C. H.; Hahn, C.; Jeong, H. E.; Yang, P. D. Si/InGaN Core/Shell Hierarchical Nanowire Arrays and Their Photoelectrochemical Properties. *Nano Lett.* **2012**, *12*, 1678–1682.
10. Cho, I. S.; Chen, Z. B.; Forman, A. J.; Kim, D. R.; Rao, P. M.; Jaramillo, T. F.; Zheng, X. L. Branched TiO_2 Nanorods for Photoelectrochemical Hydrogen Production. *Nano Lett.* **2011**, *11*, 4978–4984.
11. Sun, K.; Jing, Y.; Park, N.; Li, C.; Bando, Y.; Wang, D. Solution Synthesis of Large-Scale, High-Sensitivity ZnO/Si Hierarchical Nanoheterostructure Photodetectors. *J. Am. Chem. Soc.* **2010**, *132*, 15465–15467.
12. Lee, T. I.; Jeagal, J. P.; Choi, J. H.; Choi, W. J.; Lee, M. J.; Oh, J. Y.; Kim, K. B.; Baik, H. K.; Xia, Y. N.; Myoung, J. M. Binder-Free and Full Electrical-Addressing Free-Standing Nanosheets with Carbon Nanotube Fabrics for Electrochemical Applications. *Adv. Mater.* **2011**, *23*, 4711–4715.
13. Cheng, C. W.; Liu, B.; Yang, H. Y.; Zhou, W. W.; Sun, L.; Chen, R.; Yu, S. F.; Zhang, J. X.; Gong, H.; Sun, H. D.; *et al.* Hierarchical Assembly of ZnO Nanostructures on SnO_2 Backbone Nanowires: Low-Temperature Hydrothermal Preparation and Optical Properties. *ACS Nano* **2009**, *3*, 3069–3076.
14. Bierman, M. J.; Lau, Y. K. A.; Kvit, A. V.; Schmitt, A. L.; Jin, S. Dislocation-Driven Nanowire Growth and Eshelby Twist. *Science* **2008**, *320*, 1060–1063.
15. Lau, Y. K. A.; Chernak, D. J.; Bierman, M. J.; Jin, S. Formation of PbS Nanowire Pine Trees Driven by Screw Dislocations. *J. Am. Chem. Soc.* **2009**, *131*, 16461–16471.
16. Whang, D.; Jin, S.; Wu, Y.; Lieber, C. M. Large-Scale Hierarchical Organization of Nanowire Arrays for Integrated Nanosystems. *Nano Lett.* **2003**, *3*, 1255–1259.
17. Yu, G. H.; Cao, A. Y.; Lieber, C. M. Large-Area Blown Bubble Films of Aligned Nanowires and Carbon Nanotubes. *Nat. Nanotechnol.* **2007**, *2*, 372–377.
18. Moon, G. D.; Lee, T. I.; Kim, B.; Chae, G.; Kim, J.; Kim, S.; Myoung, J. M.; Jeong, U. Assembled Monolayers of Hydrophilic Particles on Water Surfaces. *ACS Nano* **2011**, *5*, 8600–8612.
19. Javey, A.; Nam, S.; Friedman, R. S.; Yan, H.; Lieber, C. M. Layer-by-Layer Assembly of Nanowires for Three-Dimensional, Multifunctional Electronics. *Nano Lett.* **2007**, *7*, 773–777.
20. Sun, J. W.; Liu, C.; Yang, P. D. Surfactant-Free, Large-Scale, Solution-Liquid-Solid Growth of Gallium Phosphide Nanowires and Their Use for Visible-Light-Driven Hydrogen Production from Water Reduction. *J. Am. Chem. Soc.* **2011**, *133*, 19306–19309.
21. Zhu, J.; Peng, H. L.; Marshall, A. F.; Barnett, D. M.; Nix, W. D.; Cui, Y. Formation of Chiral Branched Nanowires by the Eshelby Twist. *Nat. Nanotechnol.* **2008**, *3*, 477–481.
22. Jiang, X. C.; Tian, B. Z.; Xiang, J.; Qian, F.; Zheng, G. F.; Wang, H. T.; Mai, L. Q.; Lieber, C. M. Rational Growth of Branched Nanowire Heterostructures with Synthetically Encoded Properties and Function. *Proc. Natl. Acad. Sci. U.S.A.* **2011**, *108*, 12212–12216.
23. May, S. J.; Zheng, J. G.; Wessels, B. W.; Lauhon, L. J. Dendritic Nanowire Growth Mediated by a Self-Assembled Catalyst. *Adv. Mater.* **2005**, *17*, 598–602.
24. Dick, K. A.; Deppert, K.; Larsson, M. W.; Martensson, T.; Seifert, W.; Wallenberg, L. R.; Samuelson, L. Synthesis of Branched 'Nanotrees' by Controlled Seeding of Multiple Branching Events. *Nat. Mater.* **2004**, *3*, 380–384.
25. Li, C.; Huang, L.; Snigdha, G. P.; Yu, Y. F.; Cao, L. Y. Role of Boundary Layer Diffusion in Vapor Deposition Growth of Chalcogenide Nanosheets: The Case of GeS. *ACS Nano* **2012**, *6*, 8868–8877.
26. Li, C.; Yu, Y.; Chi, M.; Cao, L. Epitaxial Nanosheet−Nanowire Heterostructures. *Nano Lett.* **2013**, *13*, 948–953.
27. Kouno, T.; Kishino, K. Well-Arranged Novel InGaN Hexagonal Nanoplates at the Tops of Nitrogen-Polarity GaN Nanocolumn Arrays. *AIP Adv.* **2012**, *2*, 012140.
28. Yan, C. Y.; Jiang, H.; Zhao, T.; Li, C. Z.; Ma, J.; Lee, P. S. Binder-Free $Co(OH)_2$ Nanoflake−ITO Nanowire Heterostructured Electrodes for Electrochemical Energy Storage with Improved High-Rate Capabilities. *J. Mater. Chem.* **2011**, *21*, 10482–10488.
29. Lee, T. I.; Lee, S. H.; Kim, Y. D.; Jang, W. S.; Oh, J. Y.; Baik, H. K.; Stampfl, C.; Soon, A.; Myoung, J. M. Playing with Dimensions: Rational Design for Heteroepitaxial p−n Junctions. *Nano Lett.* **2012**, *12*, 68–76.
30. Osada, M.; Sasaki, T. Two-Dimensional Dielectric Nanosheets: Novel Nanoelectronics from Nanocrystal Building Blocks. *Adv. Mater.* **2012**, *24*, 210–228.
31. Wang, Q. H.; Kalantar-Zadeh, K.; Kis, A.; Coleman, J. N.; Strano, M. S. Electronics and Optoelectronics of Two-Dimensional Transition Metal Dichalcogenides. *Nat. Nanotechnol.* **2012**, *7*, 699–712.
32. Li, H.; Cao, J.; Zheng, W. S.; Chen, Y. L.; Wu, D.; Dang, W. H.; Wang, K.; Peng, H. L.; Liu, Z. F. Controlled Synthesis of Topological Insulator Nanoplate Arrays on Mica. *J. Am. Chem. Soc.* **2012**, *134*, 6132–6135.
33. Kong, D. S.; Dang, W. H.; Cha, J. J.; Li, H.; Meister, S.; Peng, H. L.; Liu, Z. F.; Cui, Y. Few-Layer Nanoplates of Bi_2Se_3 and Bi_2Te_3 with Highly Tunable Chemical Potential. *Nano Lett.* **2010**, *10*, 2245–2250.
34. Akatsuka, K.; Haga, M.; Ebina, Y.; Osada, M.; Fukuda, K.; Sasaki, T. Construction of Highly Ordered Lamellar Nanostructures through Langmuir−Blodgett Deposition of Molecularly Thin Titania Nanosheets Tens of Micrometers Wide and Their Excellent Dielectric Properties. *ACS Nano* **2009**, *3*, 1097–1106.
35. Huang, X. Q.; Tang, S. H.; Mu, X. L.; Dai, Y.; Chen, G. X.; Zhou, Z. Y.; Ruan, F. X.; Yang, Z. L.; Zheng, N. F. Freestanding Palladium Nanosheets with Plasmonic and Catalytic Properties. *Nat. Nanotechnol.* **2011**, *6*, 28–32.
36. Zhang, Q.; Hu, Y. X.; Guo, S. R.; Goebl, J.; Yin, Y. D. Seeded Growth of Uniform Ag Nanoplates with High Aspect Ratio and Widely Tunable Surface Plasmon Bands. *Nano Lett.* **2010**, *10*, 5037–5042.
37. Jiang, H.; Zhao, T.; Li, C. Z.; Ma, J. Hierarchical Self-Assembly of Ultrathin Nickel Hydroxide Nanoflakes for High-Performance Supercapacitors. *J. Mater. Chem.* **2011**, *21*, 3818–3823.
38. Wang, H. L.; Casalongue, H. S.; Liang, Y. Y.; Dai, H. J. $Ni(OH)_2$ Nanoplates Grown on Graphene as Advanced Electrochemical Pseudocapacitor Materials. *J. Am. Chem. Soc.* **2010**, *132*, 7472–7477.
39. Nikoobakht, B.; Li, X. L. Two-Dimensional Nanomembranes: Can They Outperform Lower Dimensional Nanocrystals? *ACS Nano* **2012**, *6*, 1883–1887.
40. Morin, S. A.; Bierman, M. J.; Tong, J.; Jin, S. Mechanism and Kinetics of Spontaneous Nanotube Growth Driven by Screw Dislocations. *Science* **2010**, *328*, 476–480.

41. Srinivasan, R.; Chavillon, B.; Doussier-Brochard, C.; Cario, L.; Paris, M.; Gautron, E.; Deniard, P.; Odobel, F.; Jobic, S. Tuning the Size and Color of the p-Type Wide Band Gap Delafossite Semiconductor $CuGaO_2$ with Ethylene Glycol Assisted Hydrothermal Synthesis. *J. Mater. Chem.* **2008**, *18*, 5647–5653.
42. Yu, M. Z.; Natu, G.; Ji, Z. Q.; Wu, Y. Y. p-Type Dye-Sensitized Solar Cells Based on Delafossite $CuGaO_2$ Nanoplates with Saturation Photovoltages Exceeding 460 mV. *J. Phys. Chem. Lett.* **2012**, *3*, 1074–1078.
43. Morin, S. A.; Jin, S. Screw Dislocation-Driven Epitaxial Solution Growth of ZnO Nanowires Seeded by Dislocations in GaN Substrates. *Nano Lett.* **2010**, *10*, 3459–3463.
44. Renaud, A.; Chavillon, B.; Le Pleux, L.; Pellegrin, Y.; Blart, E.; Boujtita, M.; Pauporte, T.; Cario, L.; Jobic, S.; Odobel, F. $CuGaO_2$: A Promising Alternative for NiO in p-Type Dye Solar Cells. *J. Mater. Chem.* **2012**, *22*, 14353–14356.
45. Ueda, K.; Hase, T.; Yanagi, H.; Kawazoe, H.; Hosono, H.; Ohta, H.; Orita, M.; Hirano, M. Epitaxial Growth of Transparent p-Type Conducting $CuGaO_2$ Thin Films on Sapphire (001) Substrates by Pulsed Laser Deposition. *J. Appl. Phys.* **2001**, *89*, 1790–1793.
46. Kawazoe, H.; Yasukawa, M.; Hyodo, H.; Kurita, M.; Yanagi, H.; Hosono, H. p-Type Electrical Conduction in Transparent Thin Films of $CuAlO_2$. *Nature* **1997**, *389*, 939–942.
47. Huang, M. H.; Mao, S.; Feick, H.; Yan, H. Q.; Wu, Y. Y.; Kind, H.; Weber, E.; Russo, R.; Yang, P. D. Room-Temperature Ultraviolet Nanowire Nanolasers. *Science* **2001**, *292*, 1897–1899.
48. Law, M.; Greene, L. E.; Johnson, J. C.; Saykally, R.; Yang, P. D. Nanowire Dye-Sensitized Solar Cells. *Nat. Mater.* **2005**, *4*, 455–459.
49. Wang, X. D.; Song, J. H.; Liu, J.; Wang, Z. L. Direct-Current Nanogenerator Driven by Ultrasonic Waves. *Science* **2007**, *316*, 102–105.
50. Ling, B.; Zhao, J. L.; Sun, X. W.; Tan, S. T.; Kyaw, A. K. K.; Divayana, Y.; Dong, Z. L. Color Tunable Light-Emitting Diodes Based on p(+)-Si/p-$CuAlO_2$/n-ZnO Nanorod Array Heterojunctions. *Appl. Phys. Lett.* **2010**, *97*, 013101.
51. Wang, F.; Seo, J. H.; Ma, Z. Q.; Wang, X. D. Substrate-Free Self-Assembly Approach toward Large-Area Nanomembranes. *ACS Nano* **2012**, *6*, 2602–2609.
52. Meng, F.; Morin, S. A.; Forticaux, A.; Jin, S. Screw Dislocation Driven Growth of Nanomaterials. *Acc. Chem. Res.* **2013**, *46*, 1616–1626.
53. Meng, F.; Morin, S. A.; Jin, S. Rational Solution Growth of α-FeOOH Nanowires Driven by Screw Dislocations and Their Conversion to α-Fe_2O_3 Nanowires. *J. Am. Chem. Soc.* **2011**, *133*, 8408–8411.
54. Meng, F.; Jin, S. The Solution Growth of Copper Nanowires and Nanotubes Is Driven by Screw Dislocations. *Nano Lett.* **2012**, *12*, 234–239.
55. Wang, L. S.; Tsan, D.; Stoeber, B.; Walus, K. Substrate-Free Fabrication of Self-Supporting ZnO Nanowire Arrays. *Adv. Mater.* **2012**, *24*, 3999–4004.
56. Morin, S. A.; Amos, F. F.; Jin, S. Biomimetic Assembly of Zinc Oxide Nanorods onto Flexible Polymers. *J. Am. Chem. Soc.* **2007**, *129*, 13776–13777.
57. Pokroy, B.; Kang, S. H.; Mahadevan, L.; Aizenberg, J. Self-Organization of a Mesoscale Bristle into Ordered, Hierarchical Helical Assemblies. *Science* **2009**, *323*, 237–240.
58. Morin, S. A.; Forticaux, A.; Bierman, M. J.; Jin, S. Screw Dislocation-Driven Growth of Two-Dimensional Nanoplates. *Nano Lett.* **2011**, *11*, 4449–4455.
59. Benko, F. A.; Koffyberg, F. P. The Optical Interband-Transitions of the Semiconductor $CuGaO_2$. *Phys. Status Solidi A* **1986**, *94*, 231–234.
60. Kim, S. H.; Kim, H. K.; Seong, T. Y. Effect of Hydrogen Peroxide Treatment on the Characteristics of Pt Schottky Contact on n-Type ZnO. *Appl. Phys. Lett.* **2005**, *86*, 112101.